Volume 4
Number 3
May 2026
Pages 853-1148

RSC Applied Polymers

rsc.li/RSCApplPolym

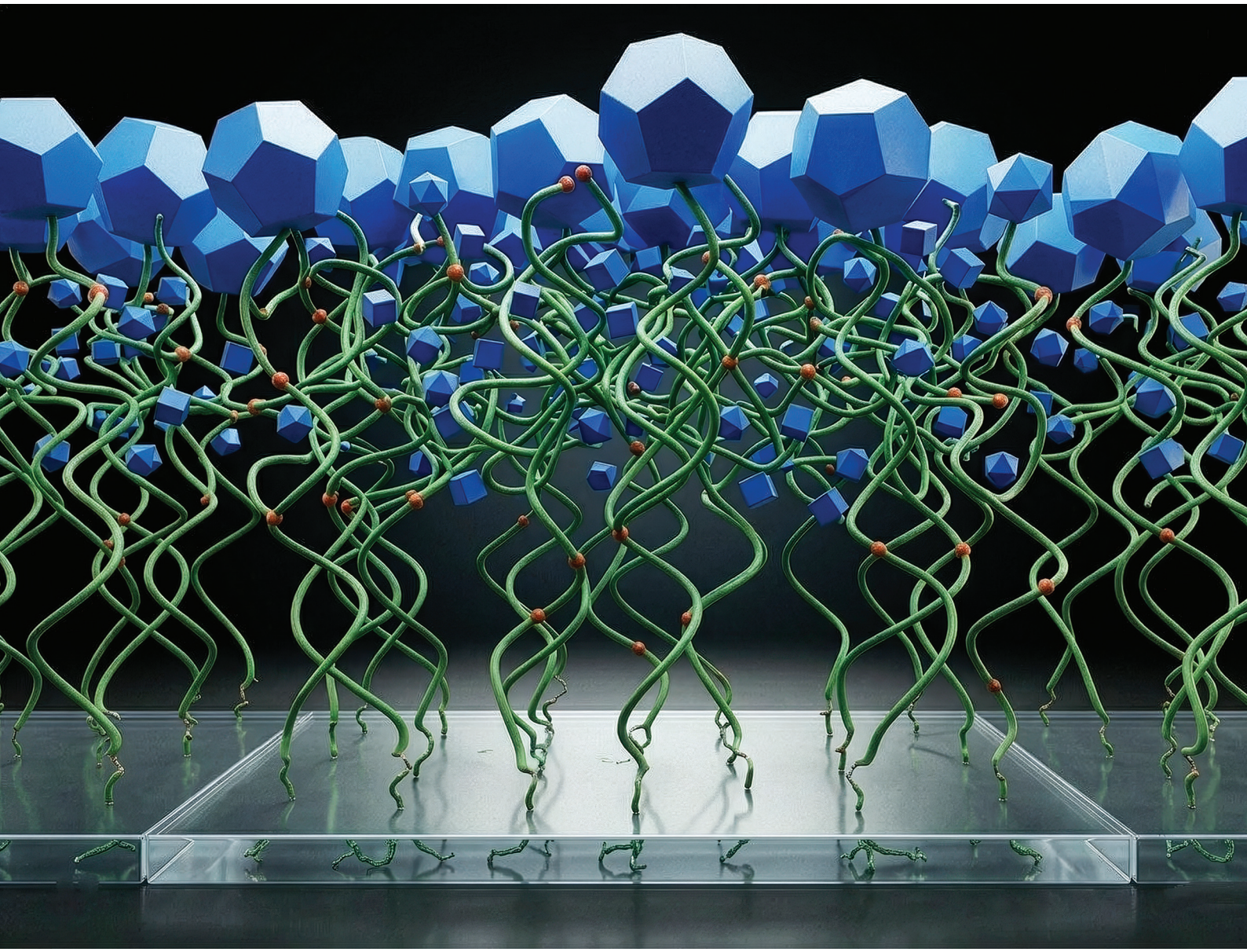

ISSN 2755-371X

ROYAL SOCIETY OF CHEMISTRY

PAPER
Agustín Iborra *et al.*
Copolymers with tailored microstructure as versatile platforms for ZIF-8 polyMOF growth

RSC Applied Polymers

PAPER

View Article Online
View Journal | View Issue

Cite this: *RSC Appl. Polym.*, 2026, **4**, 952

Copolymers with tailored microstructure as versatile platforms for ZIF-8 polyMOF growth

M. Celeste Legarto,[a,b] Agustín Iborra,*[a] Juan J. Romero,†[a] Juan M. Padró,[a] Cristian Villa Pérez,[a] Matías Rafti,[b] Isabel N. Vega[a] and Juan M. Giussi[a]

In this work, we report copolymers based on zinc dimethacrylate (ZnDMA) and poly(ethylene glycol) methyl ether methacrylate (PEGMA) as versatile platforms for the *in situ* growth of ZIF-8 polyMOFs. ZnDMA is a suitable monomer which can potentially optimize polyMOF growth, enabling improved control over the nucleation process and both final structure and morphology. The copolymers were synthesized both as bulk materials from precursor solutions and *via* surface-initiated Atom Transfer Radical Polymerization (ATRP). The composition and microstructure were investigated using the Fineman-Ross method, complemented by characterization through X-ray photoelectron spectroscopy (XPS), proton nuclear magnetic resonance (^{1}H NMR), thermogravimetric analysis (TGA), aqueous size exclusion chromatography (SEC) and scanning electron microscopy (SEM). We found that variations in structural stability, composition and microstructure of the resulting poly(ZnDMA-*co*-PEGMA)@ZIF-8 materials can be traced back to conditions affecting polyMOF growth, mainly regarding efficient nucleation and controlled crystalline growth. Overall, these results demonstrate that the hereby proposed synthetic approach to polyMOFs can be employed for the rational design of functional nanostructured porous materials.

Received 22nd January 2026,
Accepted 31st March 2026

DOI: 10.1039/d6lp00021e

rsc.li/rscapplpolym

Introduction

The class of porous materials known as Metal Organic Frameworks (MOFs) has attracted a great deal of attention over the past three decades due to their exceptional physicochemical properties and structural tunability. Among their most remarkable features are high specific surface areas (reaching up to 7000 $m^2\ g^{-1}$ under appropriate activation conditions),[1–3] uniform and well-defined pore sizes stemming from their crystalline architectures,[4–7] and the presence of coordinatively unsaturated metal sites that enable selective adsorption and heterogeneous catalysis.[8] These unique attributes have stimulated an exponential growth in MOF-related research, leading to a vast number of reports addressing their potential in energy storage and conversion,[9,10] selective adsorption,[11,12] carbon capture,[13] sensing/biosensing,[14] water harvesting[15,16] and remediation applications,[17] among many other cutting-edge applications. One effective strategy for overcoming challenges that have long hindered large-scale synthesis of MOFs for industrial applications (limited processability and reduced chemical robustness under common real-life operating conditions) has been their integration into polymeric scaffolds. Although the concept of combining MOFs with polymers was proposed more than two decades ago,[18] the formal introduction of the term "polyMOFs" and the recognition of these composite materials as a distinct class can be traced back to Cohen *et al.*[19] and, more broadly, to the seminal contribution of Matzger *et al.*[20] Since then, a wide range of synthetic strategies have been developed, yielding polyMOFs with diverse porous architectures, increased processability, and enhanced functionalities.[21–31]

A widely adopted strategy for the creation of polyMOFs is the partial or complete substitution of the organic linker in a given MOF structure with a polymer bearing equivalent coordination moieties in appropriate orientations, *e.g.*, replacing benzene dicarboxylate (bdc) in Zr-UiO-MOFs or Zn-IRMOFs with polyethers incorporating bdc units at predefined spacings.[19,22,30,31] The trade-off for the reduced thermal stability and increased synthetic complexity is the emergence of remarkable features in polyMOFs, such as designed hierarchical porosity and stimuli-responsiveness.[32] Furthermore, polyMOFs offer a unique pathway for the fabrication of free-standing structures, which are highly desirable in membrane technologies, including crosslinked polymeric brushes obtained *via* surface-initiated radical polymerization (SI-RAFT) on surface-functionalized nano- or microscale MOF units. This

[a]*YPF Tecnología (Y-TEC), Berisso, Buenos Aires, Argentina.*
E-mail: agustin.iborra@ypftecnologia.com
[b]*Instituto de Investigaciones Fisicoquímicas Teóricas y Aplicadas (INIFTA) – Departamento de Química – Facultad de Ciencias Exactas – Universidad Nacional de La Plata – CONICET – (1900), La Plata, Argentina*
† Present address: Institute for Integrative Biology of the Cell (I2BC), CEA, CNRS, Université Paris-Saclay, 91198 Gif-sur-Yvette, France.

concept has been successfully applied for Zn-imidazolate ZIF-8 [33] and Zr-based UiO-66-NH_2 PolyMOFs.[19,22]

On a related note, polymeric brushes exposing suitable functional moieties can be used as three-dimensional primers for MOF thin-film growth on targeted substrates.[34] Moreover, when monomers structurally analogous to the MOF organic linker are incorporated into the polymeric brush, the accessible porosity of the resulting polyMOF film can be precisely tuned by controlling the brush surface density, as demonstrated for ZIF-8 MOFs and imidazolate-functionalized surface-anchored polymeric brushes.[35] The above mentioned ZIF-8 MOF ($Zn(mim)_2$, mim^{2-} = 2-methylimidazolate)[36] is one of the most widely studied and belongs to the zeolitic imidazolate framework (ZIF) subclass, featuring a zeolite-like crystalline structure with SOD topology, highly ordered hydrophobic micropores (6 Å and 11.4 Å pore window and diameter respectively), and relatively high BET surface areas (up to 1600 $m^2 g^{-1}$). Owing to the versatility and high reproducibility of synthesis protocols,[37] the use of ZIF-8 for multiple applications has been explored, including gas storage,[38,39] separations,[40,41] heterogeneous catalysis, or chemical sensing.[42,43]

Ultimately, the rational design of these PolyMOF with hierarchical nanoarchitectures is driven by their potential for diverse applications. In particular, their tunable nanoscale porosity and robust polymer–MOF interfaces make them promising candidates for carbon capture, utilization, and storage (CCUS),[44,45] as well as for the selective separation of low molecular weight alkane/alkene/alkyne.[46] Furthermore, by optimizing the synthesis under conditions aligned with green chemistry principles, this platform offers a sustainable pathway toward the development of scalable sorbents for environmental remediation.[47]

Inspired by the ideas discussed above, we evaluated the feasibility of employing tailor-made polymeric architectures based on the combination of zinc dimethacrylate (ZnDMA) and poly(ethylene glycol)methyl ether methacrylate (PEGMA) as platforms for the controlled growth of ZIF-8 polyMOFs. Our main hypothesis is that *ad hoc* poly(ZnDMA-*co*-PEGMA) copolymers, featuring homogeneously distributed Zn^{2+} coordination centers, can act as effective nucleation points which can guide polyMOF formation. The selection of ZnDMA represents a rational and strategic approach to circumvent common limitations in polyMOF synthesis, as it offers advantages over other metallic ion precursor sources. Namely, ZnDMA-based copolymers enable uniform and high-density metal ion loading along the polymeric backbone. In addition, the dimethacrylate structure provides a rigid and sterically constrained coordination environment, preventing premature Zn^{2+} leaching into the solution before 2-methylimidazole (HmIm) ligand present can trigger *in situ* nucleation. Finally, the intrinsic ionic nature of ZnDMA modulates the local dielectric environment, potentially lowering the activation energy required for ZIF-8 nucleation compared to other non-ionic zinc-sources.

As ZnDMA homopolymers exhibited poor water solubility due to their high degree of crosslinking, PEGMA was selected as a comonomer owing to its greater water solubility. The incorporation of PEGMA aimed to increase hydrophilicity, reduce the degree of crosslinking, and enable homogeneous polymer growth both in solutions and on surfaces. To this end, we systematically evaluated the influence of polymer architecture and composition on polyMOF formation by employing ZnDMA-*co*-PEGMA copolymers synthesized under both bulk and surface-anchored conditions. The resulting materials are comparatively analyzed in terms of their structural and morphological features, providing insight into the role of metal-bearing polymer design in directing ZIF-8 polyMOF growth (Scheme 1).

Experimental section

Materials

(3-Aminopropyl)triethoxysilane (APTES, >99%), α-bromoisobutyryl bromide (BIBB, 98%), triethylamine (TEA, >99%), zinc methacrylate (ZnDMA, >99.9%), poly(ethylene glycol)methyl ether methacrylate average M_n 500 g mol^{-1} (PEGMA, >99%), *N*,*N*,*N*′,*N*″,*N*″-pentamethyldiethylenetriamine (PMDTA, >99%), copper(I) chloride (CuCl, >99%), 2,2′-bipyridyl (Bpy, >99%), ethyl 2-bromoisobutyrate (EBIB), zinc nitrate hexahydrate ($Zn(NO_3)_2{\cdot}6H_2O$, 98%) and 2-methylimidazole (HmIm, 99%), were purchased from Sigma-Aldrich, St Louis USA, and used without further purification. Ammonia (30% aqueous solution) and sodium chloride (NaCl) was obtained from Anedra (Bs. As., Argentina). Solvents dichloromethane (DCM) and methanol (MeOH) grade RPE, also from Anedra, were distilled under Na and kept with 4 A molecular sieves until used. The dialysis tubing cellulose membrane with a typical molecular weight cut-off of 14 000 was provided by Aldrich. Cover glasses of 18 mm diameter were purchased from VWR international. Prior to use, coverslips were cleaned using piranha solution (H_2SO_4 : H_2O_2 in a 1 : 4 ratio) and thoroughly rinsed with ethanol. Bovine serum albumin (BSA monomer), 2 mg mL^{-1} in a 0.9% NaCl solution containing sodic azide, M_w = 66.4 kDa; R_h = 3.5 nm acquire from Thermo Scientific® (Waltham, Massachusetts, USA). Ultra-pure water was produced using a Milli-Q® purification apparatus (Millipore, Molsheim, France).

Methods

Polymer bulk synthesis. PolyZnDMA, polyPEGMA homopolymers and four poly($ZnDMA_x$-*co*-$PEGMA_y$) copolymers-where *x* and *y* represent the mole fractions of ZnDMA and PEGMA in the feed, respectively, were synthesized *via* Atom Transfer Radical Polymerization (ATRP). EBIB was used as the initiator at 3 mol% relative to the total monomer content, while a Cu : PMDETA catalyst system (1 : 1, molar ratio) was employed at a 2.5-fold molar excess relative to EBIB (7.5-fold molar ratio to monomers). In each experiment, ZnDMA and/or PEGMA were dissolved in methanol to obtain a total monomer concentration of 10 wt% and transferred into a Schlenk tube. After catalyst addition, the mixtures were purged with nitrogen at room temperature for 60 min. The solutions were then heated

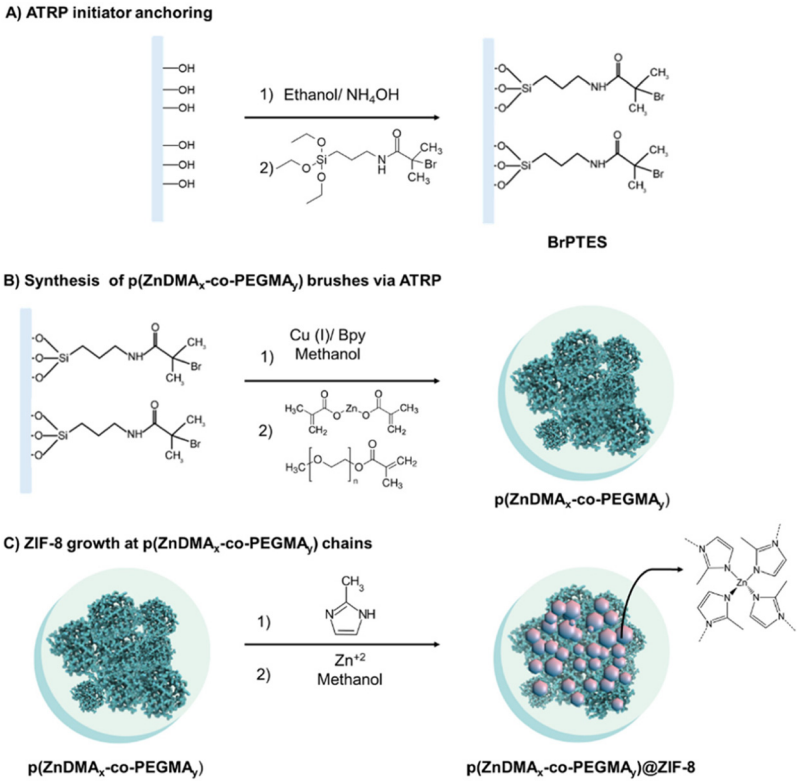

Scheme 1 Schematized procedure for sequential poly(ZnDMA$_x$-*co*-PEGMA$_y$)@ZIF-8 synthesis: (A) glass slides surface anchoring of ATRP initiator, (B) ATRP synthesis of poly(ZnDMA$_x$-*co*-PEGMA$_y$)@ZIF-8 brushes, and (C) early stages of heterogeneous nucleation and growth of ZIF-8.

to 45 °C under stirring, and EBIB was added to initiate polymerization. Reactions proceeded for 24 h. Purification of the crude homo- and copolymers was performed in two steps. First, the reaction mixtures were precipitated into hexane, and the resulting waxy solids were dried. These solids were then redissolved in water and subjected to three dialysis cycles (12 h each) against fresh distilled water using a membrane with a molecular weight cutoff of 1500 g mol^{-1} and subsequently freeze-dried. Finally, the purified polymers were lyophilized and stored until further use. The absence of olefinic proton signals in the ^{1}H NMR spectra confirmed complete monomer conversion and the high purity of the final products. The (ZnDMA : PEGMA) molar feed ratios were varied as follows: (0.1 : 1), (0.5 : 1), (1 : 1) and (1 : 0.5), corresponding to ZnDMA feed compositions (f_{ZnDMA}) of 0.1, 0.3, 0.5 and 0.7.

Polymer brushes synthesis. Poly(ZnDMA$_x$-*co*-PEGMA$_y$) copolymer brushes were grown on glass slides using a modified version of the method reported by Allegretto *et al.*[35] As the first step, an organosilane ATRP initiator, (2-bromo-2-methyl)-(triethoxysilyl)propionyloxyhexyltriethoxysilane, hereafter referred to as BrPTES, was synthesized for surface silanization (as detailed in the SI). Prior to functionalization, glass slides were activated using a freshly prepared piranha solution. The activated substrates were then placed in 50 mL reaction tubes containing 28 mL of absolute ethanol and 0.1 mL of 30% v/v aqueous NH_4OH. Subsequently, BrPTES were added and allowed to react overnight at room temperature. After silanization, the glass slides were thoroughly rinsed with ethanol and used as substrates for surface-initiated (SI) ATRP. Poly (ZnDMA$_x$-*co*-PEGMA$_y$) copolymer brushes were grown from the BrPTES-modified surfaces by immersion in previously degassed methanolic monomer solutions (10 wt%) in the presence of Cu : PMDETA (1 : 1) as the catalyst (7.5-fold molar ratio to monomers). The polymerization was conducted at 45 °C for 24 h under a nitrogen atmosphere. The reaction was terminated by exposure to air. The polymer-coated glass slides were then rinsed with MeOH and stored under vacuum until further use. As in bulk synthesis, the fraction of ZnDMA (f_{ZnDMA}) was varied as follows: 0.1, 0.3, 0.5 and 0.7.

Poly(ZnDMA$_x$-*co*-PEGMA$_y$)@ZIF-8 polyMOF synthesis. Bulk and surface-grafted poly(ZnDMA$_x$-*co*-PEGMA$_y$) copolymers were employed for polyMOF growth and are referred to as poly(ZnDMA$_x$-*co*-PEGMA$_y$)@ZIF-8-bulk and poly(ZnDMA$_x$-*co*-PEGMA$_y$)@ZIF-8-surface, respectively. Bulk synthesis involves conditions usually employed for preparation of ZIF-8 (as detailed in the SI) in the presence of 2 mg mL^{-1} suspensions of pure poly(ZnDMA-*co*-PEGMA) copolymers previously exposed to HmIm solutions. Using the same conditions and concentrations of HmIm and $Zn(NO_3)_2{\cdot}6H_2O$, surface syntheses were carried on brush-grafted substrates previously exposed to linker solutions, vertically positioned in reaction vials. After reaction time elapsed, powder and substrates were washed with fresh solvent and dried under inert atmosphere.

Proton nuclear magnetic resonance spectroscopy (^{1}H NMR). Copolymer compositions were determined by ^{1}H NMR, performed on a Bruker Ascend 500 WB spectrometer equipped with an Avance III HD console. ^{1}H NMR spectra were acquired at a resonance frequency of 500.15 MHz using 64 scans and a relaxation delay of 10 s. Raw spectrums were processed with Bruker TopSpin 3.5 pl7 software. All spectra were referenced to the residual solvent signal or internal standards (TMS in $CDCl_3$ or TMSP-d_4 in D_2O).

Aqueous size exclusion chromatography – coupled to multi-angle light scattering and differential refractive index detectors (SEC MALS-dRI). Aqueous SEC-MALS-dRI was performed to determine the average molar masses and the molar mass distributions of the polymers. The SEC-MALS-dRI system consisted of a separation module with a vacuum degasser, a quaternary pump, an autosampler, and a thermostatic column device SCL-40 System Controller (U-HPLC Nexera, Shimadzu) connected to a detector train composed of a DAWN 8 MALS detector (Wyatt Technology Corp., Santa Barbara, CA, USA) which simultaneously measured scattered light at 8 angles with nominal values ranging from 28° to 147°, followed by an Optilab differential refractive index detector (dRI) (Wyatt Technology Corp., Santa Barbara, CA, USA). For this, the 90° detector was previously calibrated with toluene, a highly scattering solvent with a known Rayleigh ratio, according to the manufacturer's instructions obtaining a calibration constant equal to 5.8293×10^{-5} ($1\ V^{-1}\ cm^{-1}$). To set the alignment and band broadening parameters for SEC-MALS experiments as well as the normalization coefficients, BSA monomer peak was used in this work. The dRI detector was calibrated with sodium chloride standards over a linear concentration range of 1–5 mg mL^{-1}, operated at room temperature and 658 nm, and yielded a calibration constant of 3.4345×10^{-5} V/Refractive-Index Unit (RIU). The separation was performed using a set of two mixed-pore size analytical SEC columns: Ultrahydrogel™ (300 × 7.8 mm, 10 μm, exclusion limit 7×10^6 Da, Waters Corporation, Milford, USA) combined with a Shodex OHPak SB-80GM column (300 × 8 mm, 13 μm, exclusion limit 2×10^7 Da, Shodex, Munich, Germany). A flow rate of 1 mL min^{-1} was used in all analyses. The column temperature was maintained at room temperature. Detector temperatures were set to 25 °C, and the injection volume was 50 μL. Samples for aqueous SEC analysis were prepared at a concentration of 2.0 mg mL^{-1}, dissolved in an aqueous 0.2 M NaCl solution, and equilibrated for at least 24 h at 30 °C prior to analysis. The addition of salts such as NaCl is generally recommended to regulate the ionic strength (IS) of the medium and to minimize secondary interactions between the analytes and the stationary phase. Prior to analysis, both samples and the mobile phase were filtered through 0.45 μm cellulose nitrate membranes (Micron Separations, Westborough, Massachusetts, USA). For all measurements, MALS and dRI data were collected and processed using ASTRA software (Wyatt Technology Corp., Santa Barbara, CA, USA, version 8.3).

Dynamic light scattering (DLS). Particle size of aqueous solutions of bulk copolymers was determined by DLS using a Zetasizer Nano Z (laser wavelength: 632 nm). The viscosity was assumed to be that of pure water at the measurement temperature (25 °C). DLS data were analyzed using distribution fitting-methods.

Raman spectrometry and wide-field optical microscopy. Raman spectra and optical micrographs were acquired using a Jasco NRS4100 microspectrometer equipped with a 900 g mm^{-1} grating and an edge filter. For Raman measurements, excitation was provided by a 20 mW green laser at 532.34 nm, while a tungsten lamp (W lamp) was used for optical microscopy. Raman signals were collected using a 20× objective (NA 0.4, Olympus) at 100% laser intensity, corresponding to approximately 6.1 mW at the sample. A circular slit (diameter = 100 μm) was employed, and the acquisition time was set to 5 s for every five averaged spectra. A silicon standard was used for wavenumber calibration.

Electron microscopy. Scanning Electron Microscopy (SEM) images and energy-dispersive X-ray spectra (EDS) were acquired using an FEI Scios 2 microscope on gold-coated specimens. TEM imaging was performed using a FEI F200X TALOS microscope operated at 200 kV. This microscope is equipped with a high brightness electron gun (X-FEG) and a four-quadrant silicon drift detector (SDD) system ("Super-X") for performing elemental analysis by means of energy dispersive X-ray spectrometry (EDXS). The high-angle annular dark-field (HAADF) STEM (Scanning-TEM) images were captured by a HAADF detector with collection angle from 22 to 136 mrad. The specimens were prepared by drop-casting and drying the as-prepared suspension on a formvar/carbon supported copper grid. Acquired images were analyzed using the image processing package FIJI software (NIH, USA).[48] Prior to analysis, the obtained images were preprocessed following a segmentation routine that included denoising, thresholding, filtering, and proper masking.[49] Particle sizes were estimated from the projected areas obtained from micrographs, assuming spherical particles, and compared to the Feret radius. Size distributions were determined considering at least 300 imaged particles per specimen. Finally, morphology descriptors were obtained by averaging the values of at least 300 particles processed under different preprocessing conditions, ensuring the robustness of the analysis.

X-ray photoelectron spectroscopy (XPS). Surface composition experiments were conducted using an EPECS FlexMode system. XPS samples were mounted on a metallic hub using conductive conducting double-sided carbon tape. Measurements were performed with an Al K^{α} monochromatic X-Ray anode run at 100 W and 10 keV, with spot size of 3.5 × 1 mm^2, and pressure maintained below 5×10^{-9} mbar. Internal calibration was carried out using the Au 4f7/2 (binding energy, BE, 84.00 eV) and the C 1s peak (BE = 284.6 eV) corresponding to adventitious carbon. To gain insight into the chemical environment of the different atoms, high-resolution XPS spectra were acquired and deconvoluted using Gaussian–Lorentzian fitting, minimizing χ^2 values.

Differential scanning calorimetry (DSC) and thermogravimetric analysis (TGA). DSC measurements were carried

out on a DSC Q2000 (TA Instruments) under nitrogen atmosphere, with heating and cooling rates of 10 °C min^{-1}, over a temperature range from −90 °C to 50 °C. Three heating–cooling cycles were performed to eliminate the thermal history of the samples. TGA analyses were conducted using a TGA Q500 (TA Instruments) under a nitrogen atmosphere, from room temperature up to 500 °C, with a purge gas flow rate of 60 mL min^{-1}.

Results and discussion

Polymer synthesis and characterization

In a previous work, we employed 1-vinylimidazole as a ligand-bearing monomer in polymeric brushes to promote ZIF-8 surface growth as a strategy to obtain ZIF-8 MOF films with tunable porosity.[35] In our synthetic approach, zinc dimethacrylate (ZnDMA) was employed as a metal-bearing monomer to promote ZIF-8 growth within the polymer scaffold, both from surface-anchored and bulk (colloidal dispersions) copolymers. Having in mind results obtained for polymerizations using different monomer compositions, we focused on determining the influence of both bulk and surface grafted poly(ZnDMA$_x$-*co*-PEGMA$_y$) scaffolds on polyMOF growth. In contrast, we employ ZnDMA which features Zn^{2+} as pre-defined nucleation sites along the polymer backbone, yielding faster growth kinetics, as no preliminary coordination step is required. This differs from ligand-bearing systems (*e.g.*, poly-vinyl-imidazole or PVI), where nucleation depends on the diffusion and coordination of Zn^{2+} ions present. Moreover, the direct involvement of polymer-bound carboxylates in metal coordination supports enhanced polymer–MOF integration, in contrast to ligand-bearing systems that typically act as scaffolds and favor surface growth.

The atom transfer radical copolymerization of zinc dimethacrylate (ZnDMA) with poly(ethylene glycol)methyl ether methacrylate (PEGMA, average M_n = 500 g mol^{-1}) yielded a series of novel copolymers whose structures, ^{1}H NMR spectra, and resonance signal assignments are presented in Fig. 1A. Four copolymers were synthesized with ZnDMA feed compositions (f_{ZnDMA}) of 0.1, 0.3, 0.5, and 0.7. To determine the compositions of the bulk copolymers, ^{1}H NMR signals corresponding to the polymer backbone of both monomers and to the PEGMA side chains were analyzed, since ZnDMA lacks side-chain groups capable of producing detectable ^{1}H NMR signals. The resonance at δ = 1.20–1.95 ppm (signal a) corresponds to the –CH_2– backbone protons of both monomers, while the signal at δ = 0.50–1.15 ppm (b) is attributed to the –CH_3 backbone protons. The peak at δ = 4.08 ppm (c) corresponds to the PEGMA –OCH_2– group bonded to the carboxylate moiety, δ = 3.65 ppm (d) is assigned to the PEGMA –CH_2O– units, δ = 3.55 ppm (e) to the terminal –OCH_2– group, and δ = 3.38 ppm (f) to the terminal –OCH_3 group of PEGMA. The copolymer compositions (F_{PEGMA}) were estimated using from the integral ratio between the PEGMA terminal –OCH_3 signal (δ = 3.4 ppm – corresponding to signal I^f) and the –CH_2– backbone signal (δ = 1.95 ppm – corresponding to signal I^b). The composition values were obtained according to eqn (1):

$$F_{ZnDMA} = 1 - F_{PEGMA} = 1 - \frac{I^f}{I^b} \quad (1)$$

For each copolymer synthesis, Table 1 shows F_{ZnDMA}, polymer conversion, the mass-average molecular weight (M_w), and the dispersity ($Đ = M_w/M_n$).

Table 1 ZnDMA mole fraction in the feed (f_{ZnDMA}), monomer conversion, ZnDMA molar fraction in the copolymer (F_{ZnDMA}), weight-average molecular weight (M_w) and dispersity ($Đ$) for the synthesized copolymers

f_{ZnDMA}	Conversion (%)	F_{ZnDMA}	M_w (g mol^{-1})	$Đ$
0.1	9.0	0.15	1.40×10^4	1.16
0.3	9.5	0.51	1.09×10^4	1.53
0.5	18.5	0.75	1.45×10^4	1.65
0.7	20.5	0.87	9.94×10^3	1.14

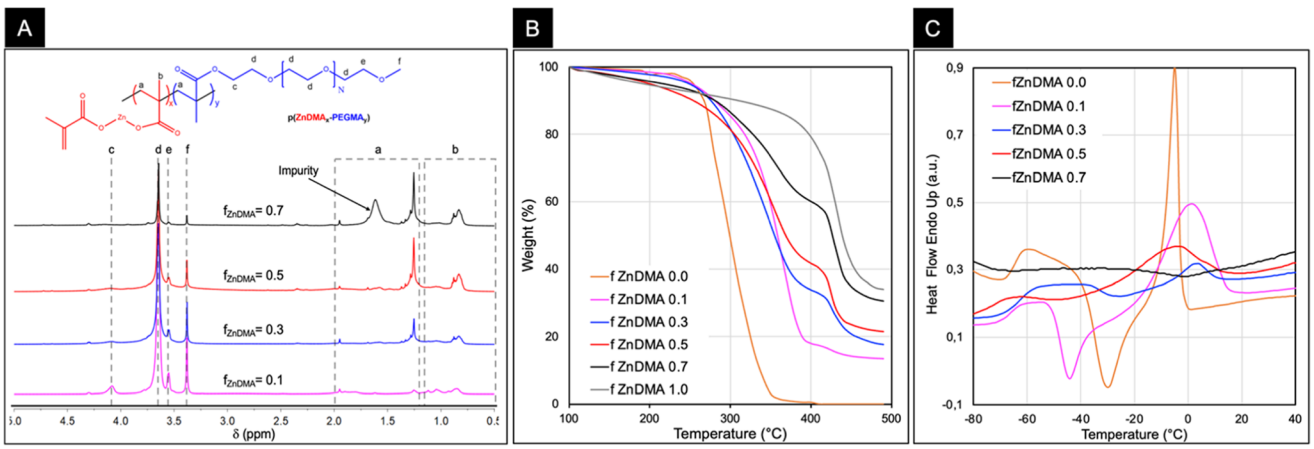

Fig. 1 (A) Generic bulk copolymers poly(ZnDMA$_x$-*co*-PEGMA$_y$) structure and their ^{1}H NMR spectra. (B) TGA curves of poly(ZnDMA$_x$-*co*-PEGMA$_y$) and homopolymers polyZnDMA and polyPEGMA. (C) DSC curves of poly(ZnDMA$_x$-PEGMA$_y$) and polyPEGMA homopolymer.

It is observed that, for the same polymerization times, increasing the proportion of ZnDMA results in higher polymerization conversion, suggesting higher reactivity of ZnDMA. The M_w values remain around 10 000 g mol^{-1} in all cases, with lower dispersity values at the compositional extremes (f_{ZnDMA} 0.1 and 0.7), close to 1.1, supporting the hypothesis of a controlled polymerization. Dispersity values closer to 1.5 for f_{ZnDMA} 0.3 and 0.5 may indicate termination mechanisms more likely associated with disproportionation or chain transfer, in agreement with theoretical predictions.[50] The thermogravimetric curves presented in Fig. 1B reveal significant differences in the initial degradation temperatures (IDT) of polyZnDMA and polyPEGMA, which are 410 °C and 260 °C, respectively. The polyZnDMA profile exhibits continuous weight loss from 100 °C up to the IDT, suggesting the presence of coordinated water molecules associated with Zn^{2+} ions, as reported by other authors.[51] As observed, the polyPEGMA homopolymer shows no residual weight at 500 °C, whereas polyZnDMA shows a residual weight of approximately 34%. This remaining weight is consistent with the formation of ZnO, as previously suggested by McNeill *et al.* for polyZnDMA degradation.[52] Furthermore, the residual weight increases as f_{ZnDMA} increases, in line with the increasing Zn^{2+} content in the copolymers. The TGA profiles of copolymers show two distinct thermal events, suggesting a block-like or sequential monomer microstructure along the copolymers chain.

DSC curves of poly(ZnDMA$_x$-*co*-PEGMA$_y$) copolymers and the polyPEGMA homopolymer exhibit complex thermal events. As previously reported, the glass transition temperature (T_g) of the polyPEGMA homopolymer is around −60 °C, and its melting temperature (T_m) is approximately −5 °C. In contrast, the polyZnDMA homopolymer does not show any detectable thermal transitions, likely due to its high degree of crosslinking.[51–53] As shown in Fig. 1C, the T_g values of the copolymers with f_{ZnDMA} = 0.1 and 0.3 remain close to −60 °C. For f_{ZnDMA} = 0.5, the T_g appears to shift slightly towards lower temperatures, while for f_{ZnDMA} = 0.7, no clear thermal transition is observed. The melting peak corresponding to PEGMA is visible for f_{ZnDMA} values of 0.1, 0.3 and 0.5. However, the high ZnDMA content in copolymer with f_{ZnDMA} = 0.7 likely suppresses the melting peak. In agreement with the TGA profile, this thermal behavior suggests a block or sequential monomer microstructure along the copolymer chains.

In comparison with bulk copolymerization, surface-initiated atom transfer radical copolymerizations (SI-ATRP) of ZnDMA with PEGMA 500 produce new brush copolymers, XPS spectra are shown in Fig. 2. Compositional analysis from the XPS data was performed by considering the C 1s and Zn 2p peak areas from the XPS survey spectra (at −284.5 and 1022.0 eV binding energies respectively). These values were corrected for adventitious carbon[54] and normalized using the corresponding atomic sensitivity factors.[55] The corrected data were then used to quantify the Zn and C contents in the sample, considering that for ZnDMA the Zn : C relation is 1 : 4. Also, from C 1s signal deconvolution, the relative contribution C species did not show significative changes, suggesting that the main contribution of this signal is related to copolymer backbone.

The F_{ZnDMA} values obtained under surface-initiated polymerization conditions were significantly different from those observed under bulk conditions, with values of 0.17, 0.34, 0.36, and 0.37 for f_{ZnDMA} = 0.1; 0.3; 0.5 and 0.7, respectively. As quantitative C determination is always challenging, XPS obtained results were compared with those derived from Raman spectroscopy, showing good agreement (as detailed in the SI).

Depth profiling studies were carried out to evaluate the homogeneity of the polymer layer and any possible lamellar segregation (see Fig. 3). A depth profiling experiment was performed for a selected poly(ZnDMA$_x$-*co*-PEGMA$_y$) surface brush corresponding to f_{ZnDMA} = 0.5 using Ar^+ ions as reactive sputtering source, and quantifying C and Si amounts form C 1s and Si 2p peaks. Considering the sharp variation in C intensity for copolymer relative to Si (glass substrate), the thickness of the polymer brush can be estimated to be below 5 nm. Furthermore, the Zn composition remained constant along the polymer brush, indicating a homogeneous distribution with no evidence of lamellar segregation.

The comonomer–copolymer composition curves (see Fig. 4) reveal distinct trends for bulk and surface polymerizations. Notable differences are observed in the copolymerization behavior of this monomer pair when comparing bulk and surface-initiated copolymerization. In bulk polymerization, there is a clear trend toward higher F_{ZnDMA} values for each corresponding f_{ZnDMA} value. In surface-initiated copolymerization, however, for low f_{ZnDMA} values, the F_{ZnDMA} values are higher than f_{ZnDMA} (0.17 > 0.1 and 0.34 > 0.3) whereas at higher f_{ZnDMA} values, the F_{ZnDMA} values become lower than f_{ZnDMA} (0.36 < 0.5 and 0.37 < 0.7).

The determination of monomer reactivity ratios provides insight into the copolymerization behavior of monomer pairs. The application of the Fineman-Ross method under the evaluated conditions allowed us to obtain the following reactivity ratios: (a) bulk condition: r_1(ZnDMA) = 3.26 and r_2(PEGMA) = 0.60; (b) surface condition: r_1(ZnDMA) = 0.13 and r_2(PEGMA) = 0.43. The obtained values, with $r_1 > r_2$ for the bulk condition, suggest a higher reactivity of the ZnDMA monomer and the preferential reaction of the poly(ZnDMA) radical toward the ZnDMA monomer. Furthermore, the product $r_1 \times r_2$ = 1.956 is consistent with an unbalanced copolymerization behavior, with a higher incorporation of ZnDMA and the possible formation of ZnDMA-enriched sequences. On the other hand, for the surface condition, the values of r_1 and r_2, together with the product $r_1 \times r_2$ = 0.055, suggest a copolymerization with a strong tendency toward cross-reactivity, meaning that each monomer would preferentially react with the other monomer rather than with itself. This is consistent with an alternating or random statistical distribution that would minimize the formation of long sequences or blocks of ZnDMA or PEGMA. It should be noted that these values are derived from a limited experimental dataset (four composition points). Nevertheless, the observed qualitative trends are considered representative of the system behavior under the studied conditions.

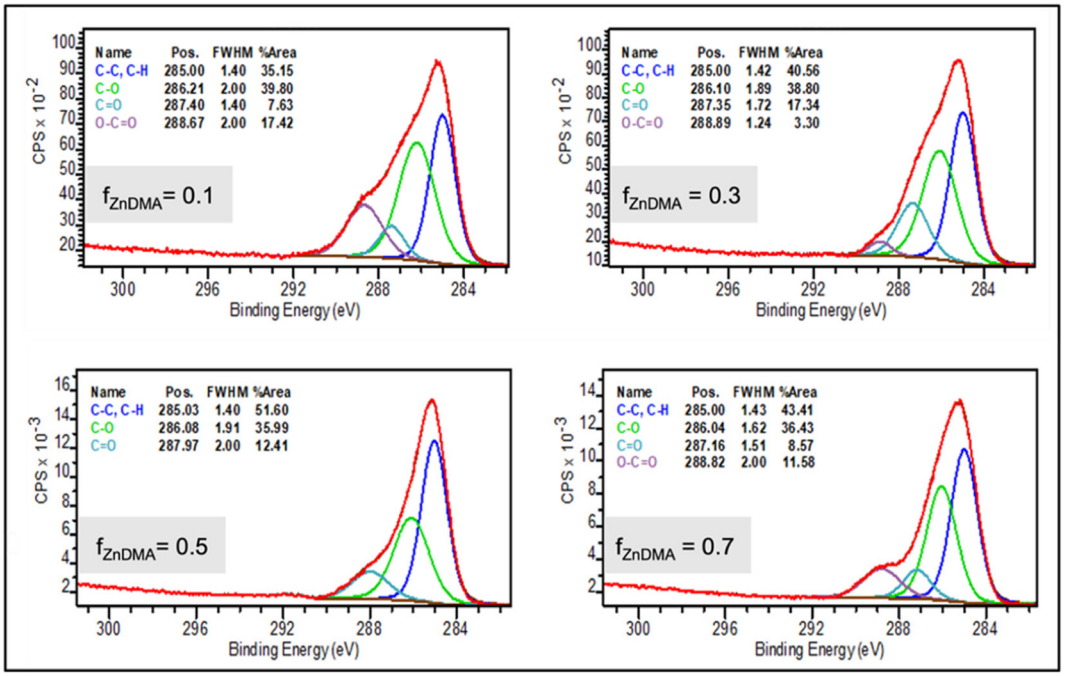

Fig. 2 XPS spectra for surface grafted poly(ZnDMA$_x$-*co*-PEGMA$_y$) copolymers with increasing f_{ZnDMA}.

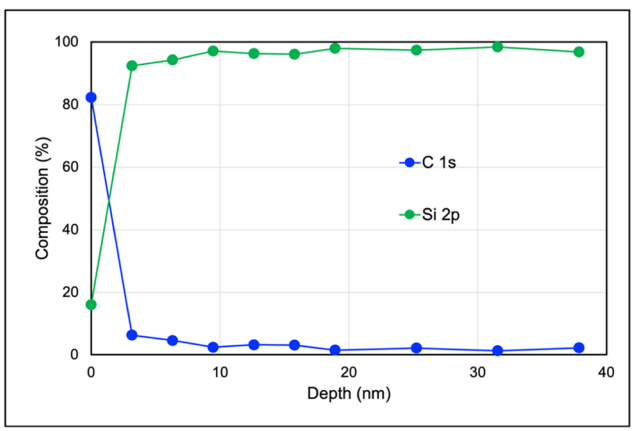

Fig. 3 Depth profile result for poly(ZnDMA$_x$-*co*-PEGMA$_y$) surface bushes corresponding to f_{ZnDMA} = 0.5.

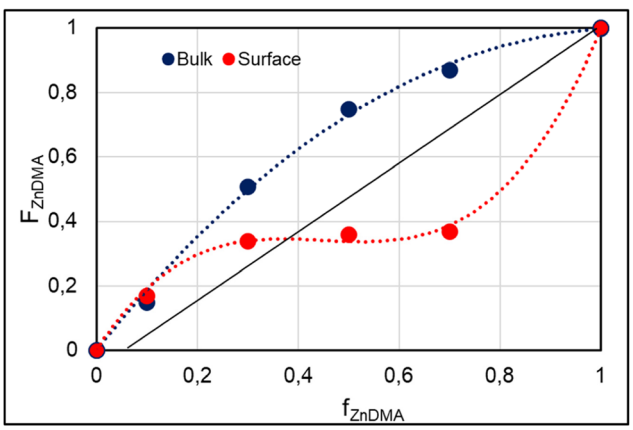

Fig. 4 Comonomer–copolymer composition curves for both bulk and surface polymerizations.

The observed change in reactivity at the film interface can be rationalized by two hypotheses: (i) an intrinsic modification of radical reactivity upon anchoring, or (ii) a differential monomer consumption, where ZnDMA, being more reactive than PEGMA, is depleted faster at the interface. The latter explanation appears more consistent, as it does not require a change in the intrinsic cross-reactivity rate constants of the monomers. Instead, the enrichment of PEGMA at the interface relative to the bulk arises from the faster depletion of ZnDMA due to its higher reactivity. Despite the operating mechanism, this change results in alternating or random statistical distribution and minimizes the formation of long sequences or blocks of ZnDMA or PEGMA as observed for bulk copolymers.

Overall, these results demonstrate that the copolymer composition can be precisely tuned *via* ATRP, although reactivity asymmetries, particularly for PEGMA in confined geometries, must be considered for predictive control. The obtained copolymers provide chemically diverse surfaces for subsequent MOF growth studies.

The poly(ZDMA$_x$-*co*-PEGMA$_y$) bulk copolymer with f_{ZnDMA} = 0.3 was selected for preparation of poly(ZDMA$_x$-*co*-PEGMA$_y$) @ZIF-8-bulk polyMOF. DLS analysis (see Fig. 5A) reveals a single size population for both the polyMOF and the bare poly (ZDMA$_x$-*co*-PEGMA$_y$) copolymer, revealing a single size population for both materials. PolyMOF particle size remains relatively constant for pH 6, 4, and 8, indicating added stability

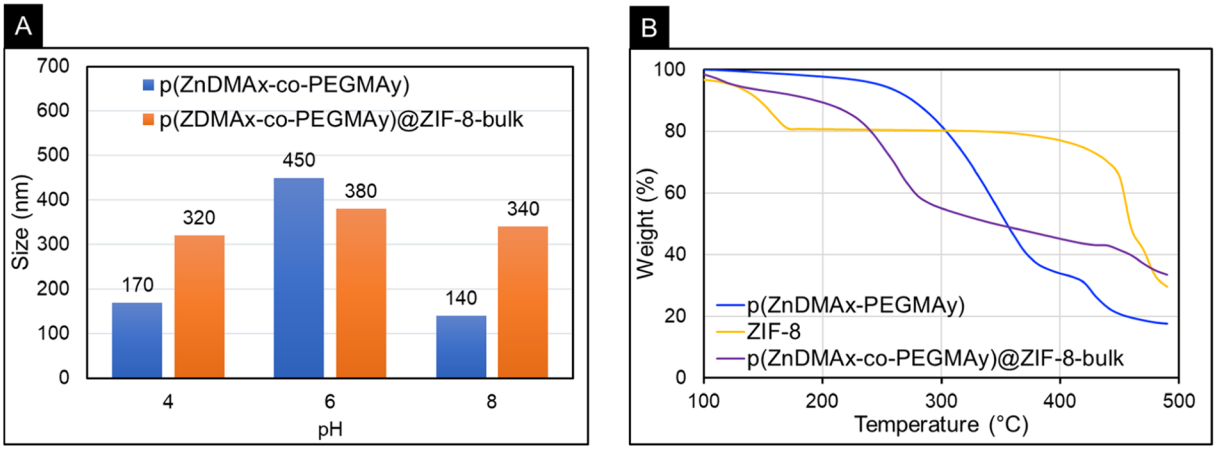

Fig. 5 (A) DLS sizes poly(ZDMA$_x$-*co*-PEGMA$_y$)@ZIF-8-bulk in comparison with poly(ZDMA$_x$-*co*-PEGMA$_y$) with f_{ZnDMA} = 0.3. (B) TGA profile of the obtained hybrid material, along with a comparison to the corresponding bulk copolymer and ZIF-8.

towards moderate acidic and alkaline conditions. This result highlights the structural robustness of the hybrid material within the well-established stability window of ZIF-8-based frameworks. In this context, pH stability was prioritized as a key operational parameter for aqueous applications. In contrast, bare polymer scaffold exhibits a size variability consistent with a crosslinking structure featuring pH-sensitive units, namely methacrylate and zinc moieties.[56,57] While pH = 6 size is approximately 450 nm, at pH = 4, partial protonation of the methacrylate –COO$^-$ groups reduce the polymer size to 170 nm, whereas for alkaline pH, partial hydroxylation of Zn^{2+} causes the polymer size to decrease down to 140 nm. Both processes modify the degree of crosslinking, leading to a significant size contraction, which is not reversible upon restitution of neutral pH conditions (see Fig. 5A).

TGA analysis (see Fig. 5B) shows the thermal profile of the polyMOF in comparison with the bare copolymer and bulk ZIF-8. Although the samples were previously dried at 60 °C, thermograms show an initial weight loss 100–150 °C corresponding to water present in ZIF-8 and polyMOF, but not in the bare polymer. According to its expected stability, ZIF-8 shows no additional thermal events until nearly 400 °C, followed by an abrupt weight loss around 450 °C, an event also present in the polyMOF. Comparison between polymer and polyMOF confirms the presence of similar features: the polymer exhibits a major weight loss near 250 °C and a smaller event around 400 °C. Both events are also present in the polyMOF, with the first one shifted slightly to lower temperatures, likely due to a thermal destabilization effect of ZIF-8 on the polymeric backbone. Aside from both DLS and TGA suggesting the successful integration of the MOF into a polyMOF composite, XRD patterns show evidence of expected diffraction peaks corresponding to ZIF-8 (as detailed in the SI). To obtain clear information regarding crystallinity, we acquired high-resolution TEM images while minimizing radiation damage for both the neat copolymer and the polyMOF samples. Wide field images were acquired under identical imaging conditions, allowing direct comparison. In the case of the polyMOF, regions with varying contrast can be observed within the same particle, which are not present in the bare copolymer. This suggests the possible inclusion of crystalline domains associated with the MOF component, due to its higher electron density. This observation is consistent with the difficulty of resolving distinct crystalline peaks in the XRD patterns. The relatively weak XRD signals observed for the polyMOF samples are to be expected due to intrinsic features of these hybrid materials, where polymer chains are interwoven within the MOF framework. This results in an effective dilution of the crystalline diffraction signal, while covalent tethering of polymer chains to metallic centers induces lattice distortion and microstrain, leading to peak broadening. In addition, polymer-induced nano-confinement may limit the growth of ZIF-8 crystallites to small domains (<10–20 nm), further reducing peak definition due to Scherrer broadening. Together, these effects are consistent with the attenuated diffraction patterns typically observed in polyMOF systems. While low-angle XRD would provide a more accurate probe of the expanded periodicities in these materials, additional HR-TEM analysis (as detailed in the SI) revealed lattice fringes of 1.6 ± 0.2 nm, confirming the presence of crystalline ordering distinct from amorphous phases or ZnO formation.

SEM analysis (see Fig. 6), which includes images corresponding to the extreme compositions (f_{ZnDMA} = 0.1 and 0.7), while images for the intermediate compositions (f_{ZnDMA} = 0.3 and 0.5) as well as bulk ZIF-8 and ZIF-8 on glass are presented in the SI, reveals a strong inverse correlation between F_{ZnDMA} and PolyMOF particle size for the surface-grafted polymeric platform (see Fig. 7); the following key aspects are proposed to rationalize such observations. The distribution of ZnDMA units is hypothesized to act as a spatial template dictating the density of nucleation sites. At high F_{ZnDMA}, the close spacing of Zn^{2+} ions is expected to generate a high local concentration, leading to rapid, simultaneous nucleation. Because the diffusing 2-methylimidazole (HmIm) ligand would be rapidly

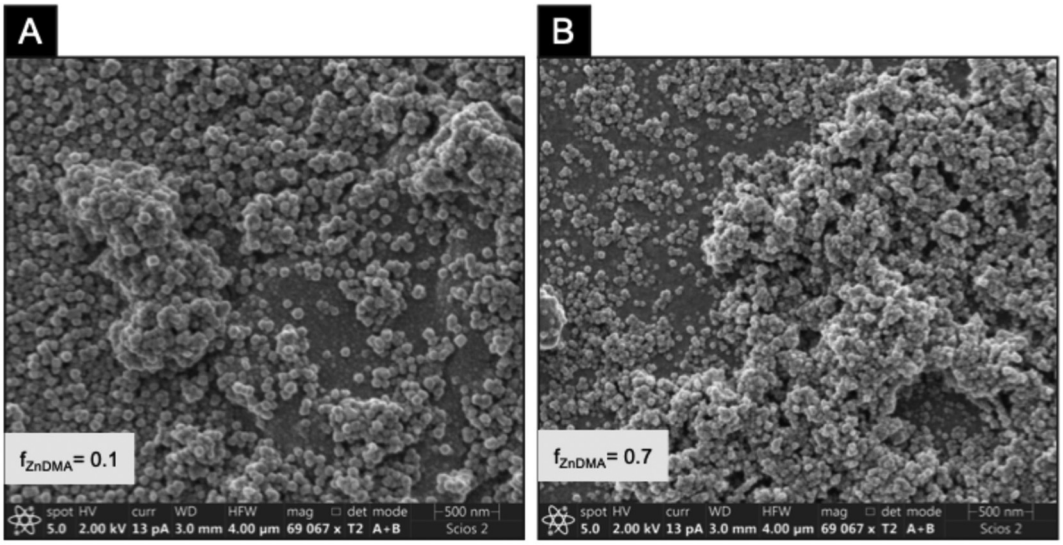

Fig. 6 (A and B) SEM image of surface grafted polyMOF on poly(ZnDMA-*co*-PEGMA)@ZIF8-surface with 0.1 and 0.7f_{ZnDMA}.

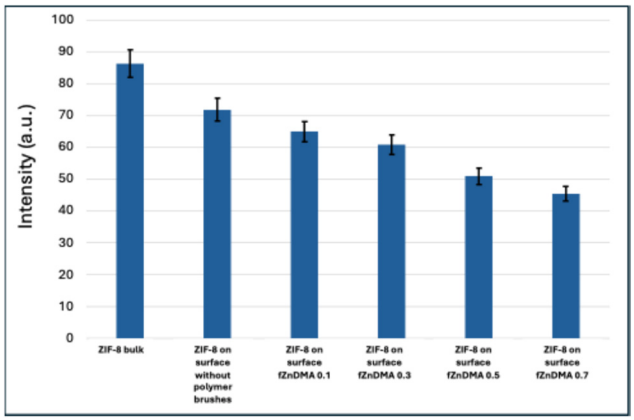

Fig. 7 Average size and polymer templating.

consumed by numerous adjacent nuclei, crystal growth may become sterically and chemically constrained, yielding smaller crystal sizes. Conversely, at low F_{ZnDMA}, the sparse distribution of Zn centers would result in fewer, isolated nuclei that can "harvest" HmIm from a larger volume, promoting larger, discrete ZIF-8 crystals.

Another aspect that may contribute is the formation of ionic clusters. Being an ionic monomer in a relatively low-dielectric polymer environment, ZnDMA is likely prone to forming ionic clusters or aggregates driven by electrostatic interactions. These clusters are proposed not to behave strictly as single atomic nucleation sites but rather as "super-nucleation sites" that could trigger the growth of polycrystalline aggregates (*e.g.*, raspberry-like structures) from a single dense ionic pocket. If these clusters are too large, Zn^{2+} ions may become partially trapped within them and thus be sterically shielded from the HmIm ligand, creating unreacted zones that could potentially compromise the mechanical integrity of the polymer–MOF interface. We further hypothesize that the interface may be governed by a nanoscale "dissolution–crystallization" mechanism; in this scenario, the interface would not correspond to a sharp boundary but rather to a gradient interpenetration region where methacrylate chains are threaded through the outer layers of the growing ZIF-8 crystals. The chain mobility (relative to the T_g during synthesis) is expected to influence how effectively ZnDMA units can rearrange to feed the growing nuclei without introducing excessive lattice strain into the MOF framework.

It is important to note that these mechanistic interpretations are inferential and consistent with the observed SEM trends, but they do not constitute direct experimental evidence. SEM primarily reflects the final morphology and does not independently resolve the nanoscale distribution of ZnDMA units or nucleation kinetics. We aim to perform experiments of scattering at wide and small angle (SAXS, WAXS) which can contribute to gain further insight on initial nucleation kinetics. Another possible way for this end would be to generate *in situ* quantitative ^{13}C-NMR or MALDI-TOF MS to resolve the precise nanoscale distribution of ZnDMA units and monomer sequence fractions.

Conclusions

This study demonstrates the successful synthesis of poly(ZnDMA-*co*-PEGMA) copolymers with tailored microstructure across the full compositional range, both in bulk and as surface-grafted polymer brushes, establishing versatile platforms for ZIF-8 polyMOF growth. Under bulk conditions, the copolymerization behavior (r_1(ZnDMA) > r_2(PEGMA)) as estimated from the Fineman-Ross analysis revealed a higher reactivity of ZnDMA and a preferential reaction of poly(ZnDMA) radicals toward the ZnDMA monomer. Consequently, the copolymerization is suggested to proceed in an unbalanced

manner, giving rise to blocky or sequential microstructures with enhanced ZnDMA incorporation and the possible formation of ZnDMA-enriched sequences, in agreement with thermal analyses. It should be noted that these reactivity ratios are derived from a limited experimental dataset (four composition points, some at moderate conversion), and therefore their absolute values may be subject to uncertainty; however, the observed qualitative trends are considered representative of the system behavior under the studied conditions. In contrast, under surface-initiated polymerization conditions, the copolymerization behavior (r_1(ZnDMA) < r_2(PEGMA) and $r_1 \times r_2 \ll 1$) suggests that the process is dominated by cross-reactivity, leading to alternating or random statistical microstructures and tending to minimize the formation of long ZnDMA or PEGMA sequences, as confirmed by X-ray photoelectron spectroscopy. This microstructural shift is proposed to enable the generation of chemically diverse polymer platforms suitable for the controlled growth of ZIF-8 polyMOFs. These mechanistic interpretations, including the relationship between copolymer microstructure and nucleation behavior, are consistent with the observed trends but remain inferential, as SEM primarily reflects the final morphology and does not directly resolve nanoscale ZnDMA distribution or nucleation kinetics. The bulk copolymer is proposed to act as an effective nucleation point for ZIF-8, yielding poly(ZnDMA$_x$-*co*-PEGMA$_y$)@ZIF-8-bulk polyMOFs that remained stable toward pH variations. In contrast, polymer brushes enabled the direct growth of ZIF-8 polyMOFs on surfaces, demonstrating that controlling F_{ZnDMA} can be used to modulate the size and surface coverage of the crystals, thereby enabling the design of polyMOF platforms with tunable nanoscale architectures. Overall, these results establish that copolymer composition and microstructure can be tuned *via* atom transfer radical polymerization and highlight the potential of ZnDMA–PEGMA copolymers as primers for the controlled growth of polyMOFs, while the proposed structure–property relationships should be interpreted in light of the aforementioned limitations and will be further explored in future studies.

Author contributions

The manuscript was written through contributions of all authors. Experimental design: M. C. L., J. M. G., J. J. R., M. R.; monomer and polymer synthesis: M. C. L., A. I., J. M. G.; performance of experiments: M. C. L., A. I., J. M. P., C. V. P.; data analysis: J. M. G., J. J. R.; writing of the first manuscript draft: M. C. L., J. J. R.; writing of manuscript: M. R., A. I., I. N. V., J. M. G.; all authors have given approval to the final version of the manuscript.

Conflicts of interest

The authors declare no competing financial interests or personal relationships that could have appeared to influence the work reported in this paper.

Data availability

The data supporting the findings of this study are available within the article and its supplementary information (SI). Additional data are available from the corresponding author upon reasonable request.

Acknowledgements

The work was performed with funds of YPF Tecnología S.A. The authors would like to thank to YPF-Tecnología S. A (Y-TEC) for giving permission for this publication and resources. MCL gratefully recognize Consejo Nacional de Investigaciones Científicas y Técnicas (CONICET), Argentina, for postdoctoral fellowship. JMG, JJR, JMP, CVP and MR are researcher members of CONICET. AI, JMG, JMP, CVP, INV and JJR working at Y-TEC.

References

1 R. Robson, The Historical Development of the Concepts Underlying the Design and Construction of Targeted Coordination Polymers/MOFs: A Personal Account, *Chem. Rec.*, 2024, **24**, 5.
2 H. C. Zhou, J. R. Long and O. M. Yaghi, Introduction to metal-organic frameworks, *Chem. Rev.*, 2012, **112**, 673–674.
3 Z. Wang, L. Liu, Z. Li, N. Goyal, T. Du, J. He, *et al.*, Shaping of Metal-Organic Frameworks: A Review, *Energy Fuels*, 2022, **36**, 2927–2944.
4 Z. Chen, K. O. Kirlikovali, P. Li and O. K. Farha, Reticular Chemistry for Highly Porous Metal-Organic Frameworks: The Chemistry and Applications, *Acc. Chem. Res.*, 2022, **55**, 579–591.
5 D. Li, A. Yadav, H. Zhou, K. Roy, P. Thanasekaran and C. Lee, Advances and Applications of Metal-Organic Frameworks (MOFs) in Emerging Technologies: A Comprehensive Review, *Global Challenges*, 2024, **8**, 2300244.
6 O. K. Farha, I. Eryazici, N. C. Jeong, B. G. Hauser, C. E. Wilmer, A. A. Sarjeant, *et al.*, Metal-organic framework materials with ultrahigh surface areas: Is the sky the limit?, *J. Am. Chem. Soc.*, 2012, **134**, 15016–15021.
7 H. Furukawa, N. Ko, Y. B. Go, N. Aratani, S. B. Choi, E. Choi, *et al.*, Ultrahigh porosity in metal-organic frameworks, *Science*, 2010, **329**, 4242–4428.
8 Z. Wang, Y. Cheng, C. Wang, R. Guo, J. You and H. Zhang, Optimizing the performance of Fe-based metal-organic frameworks in photo-Fenton processes: Mechanisms, strategies and prospects, *Chemosphere*, 2023, **339**, 139673.
9 L. G. Gordeeva, Y. D. Tu, Q. Pan, M. L. Palash, B. B. Saha, Y. I. Aristov, *et al.*, Metal-organic frameworks for energy conversion and water harvesting: A bridge between thermal engineering and material science, *Nano Energy*, 2021, **84**, 105946.

10 X. Zhang, M. Yan, P. Chen, J. Li, Y. Li, H. Li, *et al.*, Emerging MOFs, COFs, and their derivatives for energy and environmental applications, *Innovation*, 2025, **6**, 100778.
11 M. Xu, P. Cai, S. S. Meng, Y. Yang, D. S. Zheng, Q. H. Zhang, *et al.*, Linker Scissoring Strategy Enables Precise Shaping of Metal–Organic Frameworks for Chromatographic Separation, *Angew. Chem., Int. Ed.*, 2022, **61**, 37.
12 S. K. Firooz and D. W. Armstrong, Metal-organic frameworks in separations: A review, *Anal. Chim. Acta*, 2022, **1234**, 340208.
13 Y. R. Tao and H. J. Xu, A critical review on potential applications of Metal-Organic frameworks (MOFs) in adsorptive carbon capture technologies, *Appl. Therm. Eng.*, 2024, **236**, 121504.
14 B. Mohanty, S. Kumari, P. Yadav, P. Kanoo and A. Chakraborty, Metal-organic frameworks (MOFs) and MOF composites based biosensors, *Coord. Chem. Rev.*, 2024, **519**, 2216102.
15 H. Lin, Y. Yang, Y. C. Hsu, J. Zhang, C. Welton, I. Afolabi, *et al.*, Metal–Organic Frameworks for Water Harvesting and Concurrent Carbon Capture: A Review for Hygroscopic Materials, *Adv. Mater.*, 2024, **36**, 12.
16 H. A. Almassad, R. I. Abaza, L. Siwwan, B. Al-Maythalony and K. E. Cordova, Environmentally adaptive MOF-based device enables continuous self-optimizing atmospheric water harvesting, *Nat. Commun.*, 2022, **13**, 4873.
17 J. H. Wang, F. Kong, B. F. Liu, N. Q. Ren and H. Y. Ren, Preparation strategies of waste-derived MOF and their applications in water remediation: A systematic review, *Coord. Chem. Rev.*, 2025, **533**, 216534.
18 T. Uemura, K. Kitagawa, S. Horike, T. Kawamura, S. Kitagawa, M. Mizuno, *et al.*, Radical polymerisation of styrene in porous coordination polymers, *Chem. Commun.*, 2005, **48**, 5968.
19 Z. Zhang, H. T. H. Nguyen, S. A. Miller and S. M. Cohen, PolyMOFs: A Class of Interconvertible Polymer-Metal-Organic-Framework Hybrid Materials, *Angew. Chem., Int. Ed.*, 2015, **54**, 6152–6157.
20 K. A. McDonald, J. I. Feldblyum, K. Koh, A. G. Wong-Foy and A. J. Matzger, Polymer@MOF@MOF: 'grafting from' atom transfer radical polymerization for the synthesis of hybrid porous solids, *Chem. Commun.*, 2015, **51**, 11994–11996.
21 Y. Gu, M. Huang, W. Zhang, M. A. Pearson and J. A. Johnson, PolyMOF Nanoparticles: Dual Roles of a Multivalent polyMOF Ligand in Size Control and Surface Functionalization, *Angew. Chem., Int. Ed.*, 2019, **58**, 16676–16681.
22 N. Mukherjee, A. Das, S. Mukhopadhyay, S. K. Das and T. Jana, Grafting of Polymer Brushes on MOF Surface to Achieve Proton-Conducting Membranes, *ACS Appl. Polym. Mater.*, 2024, **6**, 846–858.
23 M. H. Zahir, A. Helal and A. S. Hakeem, Hybrid polyMOF Materials Prepared by Combining an Organic Polymer with a MOF and Their Application for Solar Thermal Energy Storage, *Energy Fuels*, 2021, **35**, 10199–10209.
24 S. Fan, C. Liang, F. Feng, K. Wong, K. Wang, S. Jia, *et al.*, Polymer-MOF Network Enabling Ultrathin Coating for Post-Combustion Carbon Capture, *Angew. Chem., Int. Ed.*, 2025, **64**, 10.
25 A. K. Bindra, D. Wang and Y. Zhao, Metal–Organic Frameworks Meet Polymers: From Synthesis Strategies to Healthcare Applications, *Adv. Mater.*, 2023, **35**, e2300700.
26 X. Cui, G. Kong, S. Wei, Z. Zhang, Z. Kang and H. Guo, PolyMOF interlayers modulated interfacial polymerization of ultra-thin nanofiltration membranes with efficient and stable desalination performance, *J. Membr. Sci.*, 2024, **702**, 122780.
27 H. Kim and S. M. Cohen, Metal-Organic Frameworks Constructed from Branched Oligomers, *Inorg. Chem.*, 2024, **63**, 1853–1857.
28 F. Jin, J. Liu, Y. Chen and Z. Zhang, Tethering Flexible Polymers to Crystalline Porous Materials: A Win–Win Hybridization Approach, *Angew. Chem., Int. Ed.*, 2021, **60**, 1853–1857.
29 M. Kalaj, K. C. Bentz, S. Ayala, J. M. Palomba, K. S. Barcus, Y. Katayama, *et al.*, MOF-Polymer Hybrid Materials: From Simple Composites to Tailored Architectures, *Chem. Rev.*, 2020, **120**, 8267–8302.
30 J. M. Palomba, S. Ayala and S. M. Cohen, polyMOF Formation from Kinked Polymer Ligands via ortho-Substitution, *Isr. J. Chem.*, 2018, **58**, 1123–1126.
31 S. Ayala, Z. Zhang and S. M. Cohen, Hierarchical structure and porosity in UiO-66 polyMOFs, *Chem. Commun.*, 2017, **53**, 3058–3061.
32 S. W. Li, M. F. Hsieh, T. Hong, P. Chen, K. Osada, X. Liu, *et al.*, Block Copolymer-Stabilized Metal–Organic Framework Hybrids Loading Pd Nanoparticles Enable Tumor Remission Through Near-Infrared Photothermal Therapy, *Adv. NanoBiomed Res.*, 2024, **4**, 1.
33 Y. Katayama, M. Kalaj, K. S. Barcus and S. M. Cohen, Self-Assembly of Metal-Organic Framework (MOF) Nanoparticle Monolayers and Free-Standing Multilayers, *J. Am. Chem. Soc.*, 2019, **141**, 20000–20003.
34 M. Rafti, J. A. Allegretto, G. M. Segovia, J. S. Tuninetti, J. M. Giussi, E. Bindini, *et al.*, Metal-organic frameworks meet polymer brushes: Enhanced crystalline film growth induced by macromolecular primers, *Mater. Chem. Front.*, 2017, **1**, 2256–2260.
35 J. A. Allegretto, A. Iborra, J. M. Giussi, C. von Bilderling, M. Ceolín, S. Moya, *et al.*, Growth of ZIF-8 MOF Films with Tunable Porosity by using Poly (1-vinylimidazole) Brushes as 3D Primers, *Chem. – Eur. J.*, 2020, **26**, 12388–12396.
36 K. S. Park, Z. Ni, A. P. Côté, J. Y. Choi, R. Huang, F. J. Uribe-Romo, *et al.*, Exceptional chemical and thermal stability of zeolitic imidazolate frameworks, *Proc. Natl. Acad. Sci. U. S. A.*, 2006, **103**, 10186–10191.
37 J. A. Allegretto, D. Onna, S. A. Bilmes, O. Azzaroni and M. Rafti, Unified Roadmap for ZIF-8 Nucleation and Growth: Machine Learning Analysis of Synthetic Variables

and Their Impact on Particle Size and Morphology, *Chem. Mater.*, 2024, **36**, 5814–5825.

38 D. Fairen-Jimenez, S. A. Moggach, M. T. Wharmby, P. A. Wright, S. Parsons and T. Düren, Opening the gate: Framework flexibility in ZIF-8 explored by experiments and simulations, *J. Am. Chem. Soc.*, 2011, **133**, 8900–8902.

39 C. O. Ania, E. García-Pérez, M. Haro, J. J. Gutiérrez-Sevillano, T. Valdés-Solís, J. B. Parra, *et al.*, Understanding gas-induced structural deformation of ZIF-8, *J. Phys. Chem. Lett.*, 2012, **3**, 1159–1164.

40 J. Cousinsaintremi, T. Rémy, V. Vanhunskerken, S. Vandeperre, T. Duerinck, M. Maes, *et al.*, Biobutanol separation with the metal-organic framework ZIF-8, *ChemSusChem*, 2011, **4**, 1074–1077.

41 M. Bergaoui, M. Khalfaoui, A. Awadallah-F and S. Al-Muhtaseb, A review of the features and applications of ZIF-8 and its derivatives for separating CO2 and isomers of C3- and C4- hydrocarbons, *J. Nat. Gas Sci. Eng.*, 2021, **96**, 104389.

42 Y. Sun, T. Shu, J. Ma, Q. Dai, P. Peng, Z. Zhou, *et al.*, Rational Design of ZIF-8 for Constructing Luminescent Biosensors with Glucose Oxidase and AIE-Type Gold Nanoclusters, *Anal. Chem.*, 2022, **94**, 3408–3417.

43 A. Paul, I. K. Banga, S. Muthukumar and S. Prasad, Engineering the ZIF-8 Pore for Electrochemical Sensor Applications-A Mini Review, *ACS Omega*, 2022, **7**, 26993–27003.

44 D. M. D'Alessandro, B. Smit and J. R. Long, Carbon dioxide capture: Prospects for new materials, *Angew. Chem., Int. Ed.*, 2010, **49**, 6058–6082.

45 S. R. Venna and M. A. Carreon, Highly permeable zeolite imidazolate framework-8 membranes for CO 2/CH4 separation, *J. Am. Chem. Soc.*, 2010, **132**, 76–78.

46 H. Bux, F. Liang, Y. Li, J. Cravillon, M. Wiebcke and J. Caro, Zeolitic imidazolate framework membrane with molecular sieving properties by microwave-assisted solvothermal synthesis, *J. Am. Chem. Soc.*, 2009, **131**, 16000–16001.

47 N. S. Bobbitt, M. L. Mendonca, A. J. Howarth, T. Islamoglu, J. T. Hupp, O. K. Farha, *et al.*, Metal-organic frameworks for the removal of toxic industrial chemicals and chemical warfare agents, *Chem. Soc. Rev.*, 2017, **46**, 3357–3385.

48 J. Schindelin, I. Arganda-Carreras, E. Frise, V. Kaynig, M. Longair, T. Pietzsch, *et al.*, Fiji: An open-source platform for biological-image analysis, *Nat. Methods*, 2012, **9**, 676–682.

49 J. J. Romero, M. C. De Rossi, C. Oses, C. V. Echegaray, P. Verneri, M. Francia, *et al.*, Nucleus-cytoskeleton communication impacts on OCT4-chromatin interactions in embryonic stem cells, *BMC Biol.*, 2022, **20**, 6.

50 E. Mastan and S. Zhu, A Molecular Weight Distribution Polydispersity Equation for the ATRP System: Quantifying the Effect of Radical Termination, *Macromolecules*, 2015, **48**, 18.

51 A. B. Samui, V. G. Dalvi, L. Chandrasekhar, M. Patri and B. C. Chakraborty, Interpenetrating polymer networks based on nitrile rubber and metal methacrylates, *J. Appl. Polym. Sci.*, 2006, **99**, 5.

52 I. C. McNeill, M. Zulfiqar and C. Urie, Thermal degradation of zinc polymethacrylate and a zinc methacrylate/methyl methacrylate copolymer, *Polym. Degrad. Stab.*, 1984, **9**, 239–250.

53 T. Kos, A. Anžlovar, D. Pahovnik, E. Žagar, Z. C. Orel and M. Žigon, Zinc-containing block copolymer as a precursor for the in situ formation of nano ZnO and PMMA/ZnO nanocomposites, *Macromolecules*, 2013, **46**, 17.

54 B. P. Payne, M. C. Biesinger and N. S. McIntyre, X-ray photoelectron spectroscopy studies of reactions on chromium metal and chromium oxide surfaces, *J. Electron Spectrosc. Relat. Phenom.*, 2011, **184**, 1–2.

55 J. H. Scofield, TID-4500, UC-34 Physics THEORETICAL PHOTOIONIZATION CROSS SECTIONS FROM I TO 1500 keV. UCRL-51326. 1973.

56 M. Eren and H. K. Can, Preparation of zinc methacrylate-methylmethacrylate-butyl acrylate emulsions and their application in exterior paints, *Prog. Org. Coat.*, 2019, **135**, 424–437.

57 Y. Zhang and M. Muhammed, Critical evaluation of thermodynamics of complex formation of metal ions in aqueous solutions - VI. Hydrolysis and hydroxo-complexes of Zn^{2+} at 298.15 K, *Hydrometallurgy*, 2001, **60**, 3.